Available online at www.sciencedirect.com
SCIENCE DIRECT®
PERGAMON
International Journal of Heat and Mass Transfer 46 (2003) 2207–2218
International Journal of HEAT and MASS TRANSFER
www.elsevier.com/locate/ijhmt

Turbulent heat transfer on the stationary disk in a rotor–stator system

Z.X. Yuan, N. Saniei, X.T. Yan *

Department of Mechanical and Industrial Engineering, Southern Illinois University at Edwardsville, Edwardsville, IL 62026, USA

Received 28 March 2002; received in revised form 20 September 2002

Abstract

A combined numerical and experimental study was performed to determine the turbulent heat transfer on a stationary disk, which is situated in a close distance from a rotating disk. The RNG k–ε model and the steady-state liquid crystal technique were employed respectively in the numerical simulation and the experiment. In the range of the rotational Reynolds number from 1.42×10^5 to 3.33×10^5, the heat transfer rate on the stator and the flow characteristics in the gap between the disks are presented. The results revealed that there exists an optimum rotor–stator distance for a given Reynolds number, at which the average heat transfer on the stator reaches maximum. When the Reynolds number increases, the maximum shifts towards smaller disk-distances.

1. Introduction

Rotating disks are common geometry in engineering machineries. Noticeable examples include radial flow compressor and turbine, electrical machinery, rotating heat exchanger, disk brake and friction pump. Characteristics of fluid flow and heat transfer around/on rotating disk(s) have enjoyed constant attention from researchers over the past century. A review of relevant literature may be found in Ref. [1].

In the early studies much attention had been given to the flow characteristics around rotating disk(s) rather than the heat transfer. Batchelor considered the solution of the Navier–Stokes equations for the case of contra-rotating infinite disks in the range of $-1 \leqslant \Gamma_\Omega \leqslant 0$ [2]. Assuming similarity solutions, Batchelor produced ordinary differential equations from which he deduced the behavior of the streamlines. For $\Gamma_\Omega = 0$, i.e. the rotor–stator case, he concluded that there was a radial outflow in a thin boundary layer on the rotating disk and inflow on the stationary disk, and a rotating core of the fluid in between. However, Stewartson provided different conclusions for the same problem [3]. By his results, for low Reynolds numbers ($\Omega s^2/\nu \leqslant 40$) and $\Gamma_\Omega = 0$, there was a boundary layer on the rotating disk but none on the stationary one. There was no evidence of the core rotation predicted by Batchelor. He also carried out rudimentary experiments to verify the conclusion. A discussion about this problem can be found in [4]. For infinite disks, there are multiple solutions of the equations, of which Batchelor's and Stewartson's are both possible. For finite disks, however, the solution depends on whether the disks are open or enclosed: an enclosed rotor–stator system tends to produce Batchelor-type flow with core rotation; disks open to the ambience tend to produce Stewartson-type flow with no core rotation.

Daily and Nece [5] studied the transitional characteristics of the flow in a sealed rotor–stator system. They gave an estimated value for the rotational Reynolds number at which turbulence originates, $Re = 1.5 \times 10^5$. This is below the value of 2.8×10^5 for a free disk in air. In [6] Cooper and Reshotko found that the transition occurred in the range of $Re = 1.6 \times 10^5$–2.5×10^5 for a rotating disk next to a parallel wall.

Wagner for the first time, to the knowledge of the authors, developed an expression for the convective heat transfer coefficient from a heated rotating disk [7].

* Corresponding author. Tel.: +1-618-650-3463; fax: +1-618-650-2555.
E-mail address: xyan@siue.edu (X.T. Yan).

0017-9310/03/$ - see front matter © 2003 Elsevier Science Ltd. All rights reserved.
doi:10.1016/S0017-9310(02)00525-2

Nomenclature

A_μ	constant in Eq. (7)
A_ε	constant in Eq. (8)
C_μ	constant in RNG k–ε model
c_l	constant in Eqs. (7) and (8)
D	diameter of the disk, m
h	heat transfer coefficient, W/(m^2 K)
k	turbulent kinematic energy, J/kg
l_μ	turbulent length scale, m
l_ε	turbulent length scale, m
Nu	$= hD/\lambda$, Nusselt number
$\overline{Nu}$	average Nusselt number over the radius
P	pressure, Pa
q_w	wall heat flux, W/m^2
r	local radius, m
R	radius of the disk, m
Re	$= \Omega R^2/\nu$, rotational Reynolds number
Re_y	wall-distance-based turbulent Reynolds number, Eq. (4)
s	distance between the rotor and stator, m
T	temperature, K
T_{LC}	temperature of liquid crystal, K
T_a	ambient temperature, K
U	axial velocity component, m/s
V	radial velocity component, m/s
W	azimuthal velocity component, m/s
x	coordinate in axial direction, m
y	normal distance from cell to wall, Eq. (4), m

Greek symbols

α	inverse effective Prandtl number
ε	dissipation rate of turbulent energy, J/(kg s)
ϕ	generalized variable in Eq. (2)
κ	von Karman constant
λ	air thermal conductivity, W/(m K)
μ	molecular viscosity, kg/(m s)
μ_t	turbulent viscosity, kg/(m s)
μ_{eff}	effective viscosity, kg/(m s)
ν	kinematic viscosity, m^2/s
Ω	rotating angular speed, rad/s
ρ	air density, kg/m^3
Γ	generalized diffusion coefficient
Γ_Ω	disk angular velocity ratio, Ω_2/Ω_1

Experiments have also been carried out by others with remote infrared and liquid crystal technique to investigate the heat transfer rate on the surface of a rotating disk [8,9]. For laminar flow, the distribution of heat transfer coefficient stays high at the center and then becomes relatively constant for the rest of the surface. For turbulent flow, however, the distribution declines from the center till a minimum, then increases with a large slope towards the edge of the disk.

Kreith et al. [10] examined the effects on heat transfer of placing a stationary, adiabatic surface parallel to a heated rotating plate at variable distances using the naphthalene technique. They concluded that the presence of the stationary plate decreases the effectiveness of heat transfer from the rotating disk. Numerical simulations of laminar flow and heat transfer between a stationary and a rotating disk with throughflow showed that the flow between these disks has re-circulation zones near the locations where the air entered and exited the space between the disks, which affect the heat transfer and other flow characteristics [11]. It was found that both rotational and throughflow Reynolds numbers influence the flow structure [12]. In general, the basic unicellular structure occurs for low Reynolds number flow. With the increase of the throughflow Reynolds number, a multi-cellular flow structure may be found. The similarity solutions were also found to be inappropriate for approximating the real flow between finite disks. In shrouded rotor–stator systems, the flow transition from laminar to unsteady motion occurred abruptly at some Reynolds number, without any oscillatory behavior [13]. The heat transfer on the rotating disk was numerically and experimentally studied and compared for rotational Reynolds numbers up to 1.5×10^6 in [14]. If the rotating speed is high enough and a proper working fluid is chosen, the rotor–stator system can even be used as a heating mechanism [15].

The system of co-rotating disks is another kind of configuration with respect to rotation. It may relate to throughflow [16,17] or effect of thermal buoyancy [18]. When the axial throughflow is distributed along the radius of the disk, either wall injection or wall suction will have an appreciable effect on flow structure and heat transfer performance [19]. In the case of hot-wall/cold-fluid, the centrifugal buoyancy has a suppression effect on the skin friction and heat transfer rates. The wall conduction and wall heat capacity were incorporated into the analysis of unsteady laminar flow and heat transfer between two co-rotating disks in [20].

The last variant of rotating disks is the contra-rotating system. It seemed that at the same rotational Reynolds number the contra-rotating system tend to generate turbulent flow more easily than rotor–stator system [21,22]. Though both laminar and turbulent computations had been conducted for $2.3 \times 10^5 \leqslant Re \leqslant 1.2 \times 10^6$, laser Doppler anemometry measurements confirmed only the turbulent computations. It was also found that even for local rotational Reynolds number as

low as $\bar{r}^2 Re = 2.2 \times 10^4$ (where $\bar{r} = r/R$), laminar boundary layers formed on the disks but the radial inflow in the non-rotating core was always turbulent. The effect of the perpendicular motion of a disk in contra-rotating system on the load, torque and heat transfer are computed in [23] for low Reynolds numbers ($\Omega s^2/\nu \leqslant 100$). The shrouded sidewalls and the temperature difference between the disks can influence the flow pattern and heat transfer performance significantly. Numerical simulations to this kind of turbulent flow presented multiple results [24].

The objective of this paper is to numerically and experimentally investigate the turbulent heat transfer performance on a heated stationary disk placed at a short distance from another disk rotating at high speed. The rotating disk is kept adiabatic and used as a cooling mechanism. The effects of the rotational Reynolds number and the disk-distance on the fluid flow in between the disks and the heat transfer on the stationary disk will be addressed.

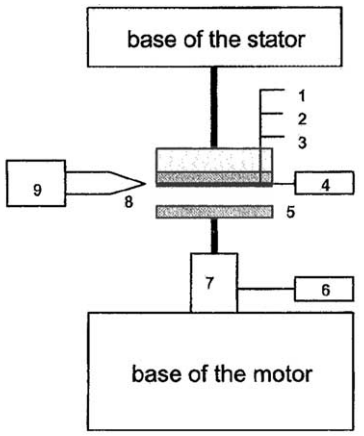

Fig. 1. Experimental apparatus.

2. Experimental methods

A steady-state liquid crystal technique was employed for detecting isotherms on the stationary disk. This technique has been described in detail by Saniei and Dini in [25]. Liquid crystal thermography is an effective technique to measure temperature. This is because that liquid crystals undergo a reversible change in color due to a change in temperature. The color change is due to the selective reflectivity of color based upon the helical structure of the crystal itself. This helical structure is quite sensitive to temperature changes. Therefore, when a temperature change occurs, the structure of the helix changes, which in turn changes the reflective properties of the crystals causing them to reflect a different wavelength of light (a different color). The temperature at which the crystals undergo this transformation is specific. This color change gives an accurate indication of temperature. When a color shows up at a given point and the corresponding temperature is T_{LC}, the heat transfer coefficient of this point is determined by

$$h(x) = \frac{q_w(x)}{T_{LC}(x) - T_a} \tag{1}$$

where $q_w(x)$ is the local convective heat flux of the wall on which the liquid crystal is coated. q_w is provided by a surface heater and determined by the power supply and the area of the disk surface. T_a denotes the ambient temperature. The liquid crystal for the current experiment was the narrowband-type R35C1W.

Fig. 1 shows the experimental system in this study. The stationary and the rotating disks were made of Plexiglas and each had a diameter of 20.5 cm. The stationary disk was 0.9 cm thick with a styrofoam insulation cover of 3.2 cm to minimize the conduction. The rotating disk was 0.9 cm thick with no insulation.

The stationary disk, which is suspended from the top, was painted black facing down. A flat heater, a model KHR 8/10 made by Omegalux, was affixed to the painted surface using rubber sealant to provide uniform heat flux boundary condition. The heater was connected to a HP6633A power supply. A grid was drawn on the heater with white ink so that the location of the color change of the liquid crystal could be observed and recorded. Micro-encapsulated liquid crystals were air-brushed on the surface of the circular heater. The rotating disk was attached to the shaft of a variable speed motor, a model 22VM51–020–5 made by Honeywell. The speed of the motor was adjusted by the amount of voltage supplied by an E&L Instrument PS-01 power supply. In addition, a thermocouple was placed near the outer edge of the upper disk to measure the ambient temperature.

Measurements were taken for disk-distances 0.5, 0.75 and 1.0 cm. Further close distances were not involved because the vibration of the rotating disk may cause the disks to collide. Once the disks had been placed at the appropriate distance, the power supply for the heater was adjusted to its appropriate value, as was the motor's speed. Then the system was allowed to reach its steady-state condition (30–60 min). A steady isotherm was observed which corresponded to a specified temperature according to the color–temperature calibration. Isotherms were observed through a mirror placed beneath the transparent rotating disk, parallel to the disk surface. Before formal measurement, the relationship between the rotational speed of the motor and its power input, as well as the resistance of the circular heater, had been

calibrated. The locations of the isotherms were recorded along with the voltage input of the motor and the current and voltage input of the heater. The ambient temperature was also recorded at the same time. Once these measurements were recorded, the power input to the heater was changed and the color ring would move to a new position correspondingly. This procedure was repeated and a series of isotherms could be obtained. The rotational speed was kept constant for each run so that isotherms could be observed at different positions on the stationary disk. After the measurements were completed for a rotational speed, a new rotational speed was selected. Once all speeds had been investigated, the disk-distance was changed and the process started once again.

Uncertainty analysis was carried out for the experimental Nusselt numbers [26]. The uncertainty of the Nusselt number ranged from 3.0% to 8.0% for different runs. It is important to note the uncertainty due to the location of the isotherms formed by the liquid crystal. As mentioned above, the color play on the disk to which the liquid crystals were applied was viewed through the rotating disk using a mirror. The closer the color ring progressed to the center of the disk, the less precision found in the location of the color ring. Near the edge of the disk, the location of the color ring was distinguishable within ±1 mm. The inmost radius on which the uncertainty was acceptable was $r/R = 0.244$, where the uncertainty of the color ring location was within ±3 mm. This increase in uncertainty is due to the fact that liquid crystals give a higher resolution when there is a large temperature gradient. Near the center, the temperature gradient is less pronounced.

3. Numerical analysis

The problem under study is a steady, axisymmetric swirling flow and heat transfer. Though many different turbulence models have been developed, e.g. two-equation model, RSM and large eddy simulation, the RNG k–ε turbulence model is usually considered a desirable selection regarding rotating or swirling flow. For weakly to moderately strained flows, the RNG model tends to give results comparable to the standard k–ε model. In rapidly strained flows, the RNG model yields a lower turbulent viscosity than the standard k–ε model. Thus, the RNG model is more responsive to the effects of rapid strain and streamline curvature than the standard k–ε model, which explains the superior performance of the RNG model for certain classes of flows including rotational flow.

The RNG k–ε turbulence model is derived from the instantaneous Navier–Stokes equations, using the "Re-Normalization Group" method [27]. The analytical derivation results in a model with constants different from those in the standard k–ε model and an additional term in the ε equation. The general form of the equations governing an axisymmetric rotating flow can be expressed as

$$\frac{\partial}{\partial x}(\rho U\phi) + \frac{1}{r}\frac{\partial}{\partial r}(\rho r V\phi) = \frac{\partial}{\partial x}\left(\Gamma\frac{\partial\phi}{\partial x}\right) + \frac{1}{r}\frac{\partial}{\partial r}\left(r\Gamma\frac{\partial\phi}{\partial r}\right) + S_\phi \qquad (2)$$

The source terms, S_ϕ, and the diffusion coefficient, Γ, for the different variables, ϕ, in the RNG k–ε model are

Table 1
Source term expressions for the different independent variables in Eq. (2) and constants in RNG k–ε model

ϕ	Source term S_ϕ	Γ
1	–	–
U	$-\frac{\partial P}{\partial x}+\frac{\partial}{\partial x}\left(\Gamma\frac{\partial U}{\partial x}\right)+\frac{1}{r}\frac{\partial}{\partial r}\left(r\Gamma\frac{\partial V}{\partial x}\right)$	μ_{eff}
V	$-\frac{\partial P}{\partial r}+\frac{\partial}{\partial x}\left(\Gamma\frac{\partial U}{\partial r}\right)+\frac{1}{r}\frac{\partial}{\partial r}\left(r\Gamma\frac{\partial V}{\partial r}\right)-2\Gamma\frac{V}{r^2}+\frac{\rho W^2}{r}$	μ_{eff}
W	$-\frac{\rho VW}{r}-\frac{W}{r^2}\frac{\partial}{\partial r}(r\Gamma)$	μ_{eff}
k	$G_k-\rho\varepsilon$	$\alpha_k\mu_{\text{eff}}$
ε	$\frac{\varepsilon}{k}(C_1G_k-C_2\rho\varepsilon)-R$	$\alpha_\varepsilon\mu_{\text{eff}}$
T	0	$\alpha_T\mu_{\text{eff}}$
	$S^2=2\left[\left(\frac{\partial U}{\partial x}\right)^2+\left(\frac{\partial V}{\partial r}\right)^2+\left(\frac{V}{r}\right)^2\right]+\left(\frac{\partial W}{\partial x}\right)^2+\left[r\frac{\partial}{\partial r}\left(\frac{W}{r}\right)\right]^2+\left(\frac{\partial U}{\partial r}+\frac{\partial V}{\partial x}\right)^2$	
	$G_k=\mu_tS^2$	
	$R=\frac{C_\mu\rho\eta^3(1-\eta/\eta_0)}{1+\beta\eta^3}\frac{\varepsilon^2}{k}$	
	$\eta=\frac{Sk}{\varepsilon}$	
	$\mu_{\text{t}}=C_\mu\rho\frac{k^2}{\varepsilon}$	
	$\mu_{\text{eff}}=\mu+\mu_{\text{t}}$	
$C_\mu=0.0845$ $C_1=1.42$ $C_2=1.68$ $\eta_0=4.38$ $\beta=0.012$		

given in Table 1. The inverse effective Prandtl number for k, ε and T is determined by

$$\left|\frac{\alpha-1.3929}{\alpha_0-1.3929}\right|^{0.6321}\left|\frac{\alpha+2.3929}{\alpha_0+2.3929}\right|^{0.3679}=\frac{\mu}{\mu_{\text{eff}}} \tag{3}$$

where $\alpha_0=1.0$ for k or ε equation and $\alpha_0=1/Pr$ for energy equation. In the high-Reynolds-number limit ($\mu \ll \mu_{\text{eff}}$), $\alpha_k=\alpha_\varepsilon=\alpha_T=1.3929$.

In consideration of the relatively drastic change of the flow pattern near the solid wall, two-layer zonal model has been adopted as near-wall treatment method in the simulation. The advantage of this method lies in that the whole domain is subdivided into a viscosity-affected region and a fully turbulent region. The demarcation of the two regions is determined by a wall-distance-based turbulent Reynolds number, Re_y, which is defined as

$$Re_y=\frac{\rho\sqrt{k}y}{\mu} \tag{4}$$

where y is the normal distance from the wall at the cell centers. In the fully turbulent region ($Re_y>200$), the RNG k–ε model is employed, while in the viscosity-affected near-wall region ($Re_y<200$), the one-equation model of Wolfshtein [28] is employed. In the one-equation model, the momentum equations and the k equation are retained as described above. However, the turbulent viscosity is computed from

$$\mu_t=\rho C_\mu\sqrt{k}l_\mu \tag{5}$$

The ε field is computed from

$$\varepsilon=\frac{k^{3/2}}{l_\varepsilon} \tag{6}$$

The length scales in Eqs. (5) and (6) are computed from [29]

$$l_\mu=c_l y\left[1-\exp\left(-\frac{Re_y}{A_\mu}\right)\right] \tag{7}$$

$$l_\varepsilon=c_l y\left[1-\exp\left(-\frac{Re_y}{A_\varepsilon}\right)\right] \tag{8}$$

The constants in above equations are: $c_l=\kappa C_\mu^{-3/4}$, $A_\mu=70$, $A_\varepsilon=2c_l$. κ is the von Karman constant, $\kappa=0.42$.

Fig. 2 shows the schematic diagram of the rotor–stator system and the simulation domain. x-axis was chosen as the axis of rotation. The disk on the right hand represents the upper stator and the one on the left represents the lower rotor. Geometries of the disks are the same as the experimental counterparts. The simulation domain takes a rectangular shape with the two half-disks located in the center of the lower edge. The width of the domain is the length of the disk diameter, while its height is equal to one and a half of the disk diameter. By trial runs, such a domain produced relatively accurate results with a moderate grid mesh. The result of grid sensitivity study showed that meshes of 168×182 and 190×212 gave average heat transfer coefficients with a difference less than 1.3%. Therefore the mesh of 168×182 was adopted in the simulation. A non-uniform grid was used to account for the high gradient of velocity and temperature in the vicinity of surfaces.

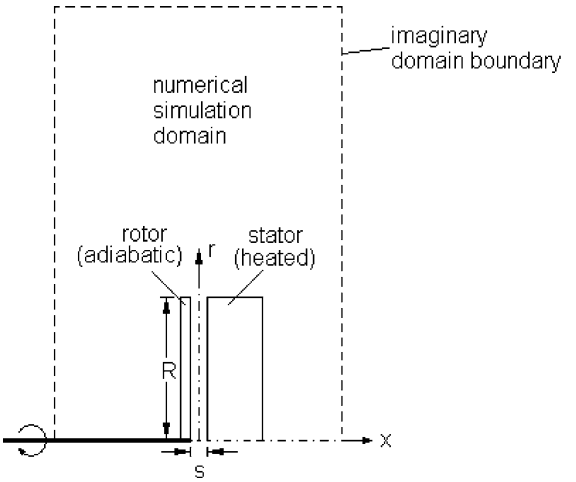

Fig. 2. Schematic diagram of the interacted rotor–stator system and its numerical simulation domain. The rotor is adiabatic. The stator is heated on its inner surface facing toward the rotor.

Thermal boundary conditions of the both disks were consistent with those of the actual experiments. Only the inside surface of the stator was heated with a uniform heat flux. Other surfaces, of both the rotor and the stator, were kept adiabatic. A special attention was paid to the boundary conditions on the imaginary domain border. It is impossible to give the actual velocity components to this boundary. But it is plausible to give it a gauge pressure of zero in the simulation. A 5% in the turbulence intensity and a value of 10 for the turbulence viscosity ratio (μ_t/μ) have been defaulted for the possible backflow on this boundary.

SIMPLE algorithm incorporated in the FLUENT, version 5.5, was adopted to solve this pressure–velocity coupled problem. The second order upwind scheme was employed for discretization of the physical parameters except for the pressure corrective equation. As to the pressure corrective equation, PRESTO! scheme was used. This is a method of pressure interpolation that is similar to the staggered grid schemes used with structured meshes [30]. The PRESTO! scheme provides improved pressure interpolation in situations where large body forces or strong pressure variation are present in swirling flows. During the process of calculation, the residual of every equation was monitored. The convergence criterion is 10^{-8} for energy equation and 10^{-3} for the others.

4. Results and discussion

4.1. Flow pattern and temperature field

Fig. 3 shows the flow patterns around the rotor–stator system as Reynolds number changes from 1.42×10^5 to 3.33×10^5 for a fixed disk-distance $s = 0.75$ cm. Comparing with the cases of single rotating disk [8] or co-rotating disks [19], the flow patterns here are deflected towards the stationary disk instead of presenting symmetrical streamlines. As the Reynolds number increases, the deflection becomes more obvious. Influenced by the pumping function of the rotor, the airflow in vicinity of the stator travels around its corners and is sucked into the gap between the disks. Streamlines on the left side of the rotor are almost drawn perpendicularly toward the surface of the disk, while those on the right side of the stator are sucked onto the surface with large angles. Another interesting phenomenon is the vortical eyes. There exists a vortical eye for each of the high Reynolds number cases of $Re = 2.94 \times 10^5$ and 3.33×10^5. Their distances from the outer edge of the stator are $0.263D$ and $0.184D$ respectively. These vortical eyes indicate that the turbulent intensity is strengthened as Reynolds number increases.

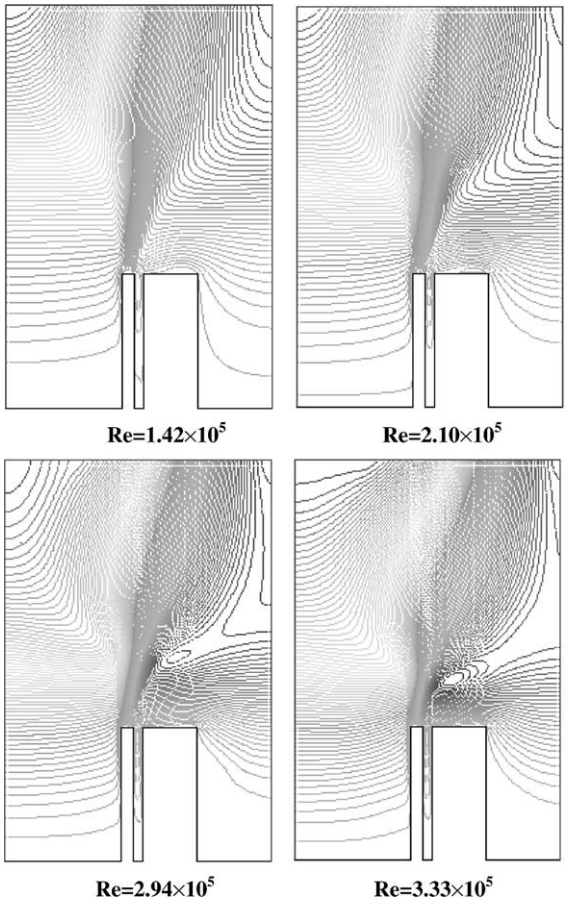

Fig. 3. Flow pattern around the rotating–stationary disk system at different Reynolds numbers. Disk-distance is 0.75 cm.

In order to see clearly the flow pattern and the temperature changes in the gap between the disks, a blow-up plot of streamline and temperature is shown in Fig. 4. There are two re-circulating regions around the corners of the stationary disk (Fig. 4(a)): one on the top and the other just down into the gap. These re-circulating regions formed as a result of the flow separation around the sharp corners. Though the re-circulating region down into the gap is much smaller than the one on the top, it has a strong influence on heat transfer on the stator. This feature will be discussed in the following sections. In general, the flow pattern inside the gap belongs to the Stewartson-type, where there is no evidence of rotating core inside the gap but for a small one near the opening. In the gap streamlines densely stuck to the surface of the rotor, while those near the stator are sparsely distributed. Together with the radial and azimuthal velocity distributions in Figs. 5 and 7, it is clear that there exists a boundary layer on the rotor but none on the stator. The flow is outward in the boundary layer on the rotor and it is mainly inward near the stator. This is just an actual verification of the theory of Zandbergen and Dijkstra [4], which stated that for finite disks, a system open to the ambience tends to produce Stewartson-type flow pattern. Similar streamline patterns are also found in the other cases.

Fig. 4(b) represents the distribution of the isotherms in the gap. Outside the gap there was no apparent temperature rise over that of the ambient air. The temperature of the ambient air is kept at 300 K. It can be seen that the changes of the temperature are uneven: it increases slowly in the outer half part and quickly in the center part. The temperature rise at the midway of the centerline is less than 3 °C, while it reaches over 15 °C near the rotational axis. Since less airflow can penetrate into the depth of the gap passage, the section near the axis is not cooled as effectively as the outer section.

4.2. Characteristics of the velocities and temperature inside the gap

Acting as a barrier, the stationary disk blocks the flow pumped by the rotating disk. Thus the unique feature of the flow in a rotor–stator system is the asymmetry of the distributions of the physical variables. A typical case, $s = 1.0$ cm, $Re = 3.33 \times 10^5$, is taken here for discussion. Fig. 5 presents the distributions of the radial velocity component, V, along the rotational axis at five radii inside the gap. It is interesting to see that all profiles of the radial component cross the point of

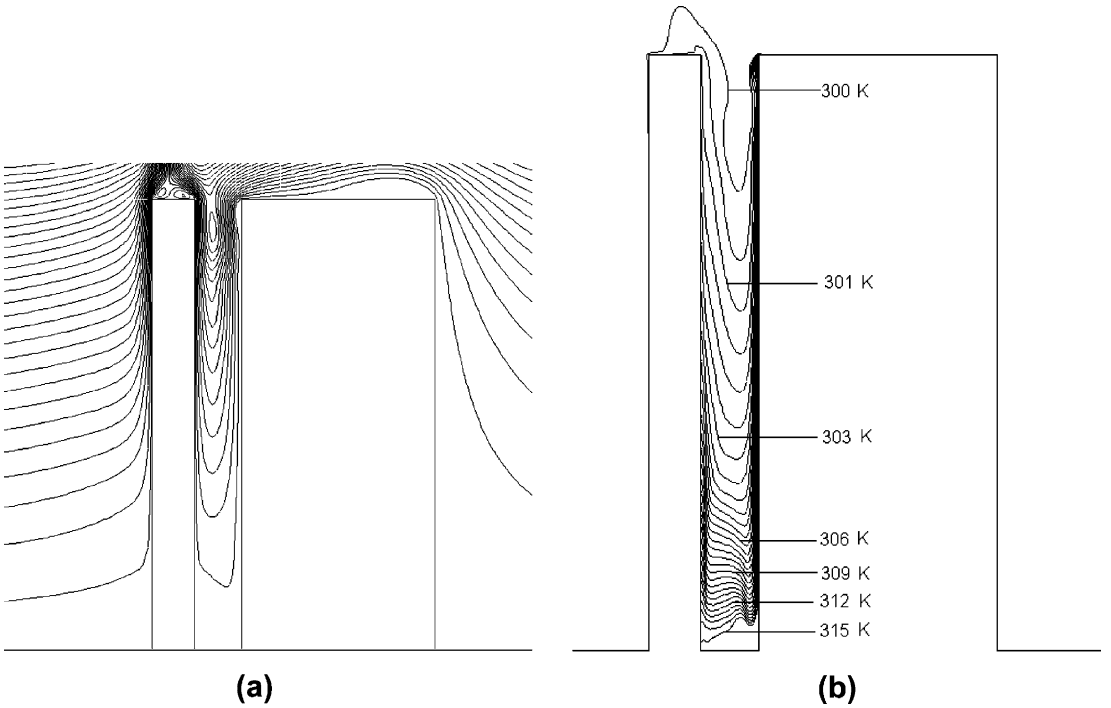

Fig. 4. Blow-up of the flow field and temperature profile in the gap between the rotor and the stator ($Re = 3.33 \times 10^5$, $s = 1.0$ cm). (a) Flow field; (b) temperature profile.

$x/s = -0.14$. In the right part from this point the flow is mainly negative, indicating that the air flows inwards. From the inlet of the gap to the axis the radial velocity decreases gradually, till $r/D = 0.1$ a very small positive velocity occurs in the central part. As to the situation in the vicinity of the stator wall ($x/s = 0.5$), the changes of the velocity become a little complicated. Opposite to the negative values of $r/D = 0.1$–0.4, the velocity for $r/D = 0.488$ is positive. This indicates the existence of a local re-circulating region, which is consistent with the separated region around the inlet corner in Fig. 4(a). In the left part from the crossing point, all velocities are positive, meaning outward flows. The velocity becomes greater as it flows outward. For each profile of r/D there exists a maximum of radial velocity, which is located approximately at $x/s = -0.46$.

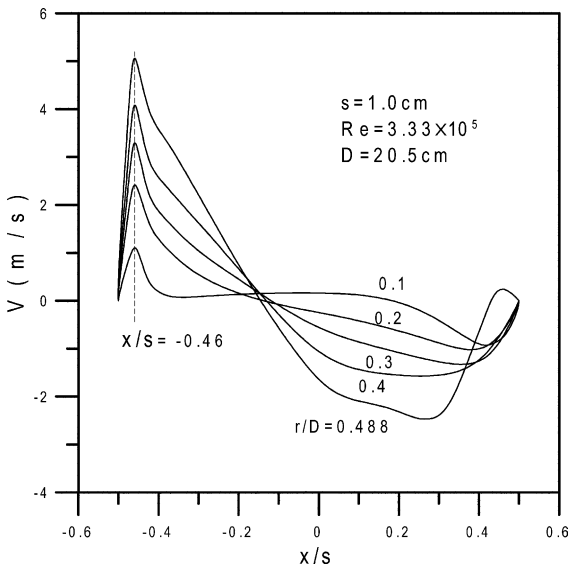

Fig. 5. Radial velocity component inside the gap between the rotor and the stator.

The axial velocity component U is shown in Fig. 6. This velocity component is much smaller than the radial one. The curves for $r/D = 0.1$–0.4 are similar patterns, except for $r/D = 0.4$ being with a positive part near the inlet. Negative velocities mean that the air flows from the stator toward the rotor. The axial velocities for $r/D = 0.1$–0.4 reach their minimum in the range of $x/s = -0.2$–0. Differences among them are small for $x/s < -0.2$ but obvious for $x/s > -0.2$. The profile for $r/D = 0.488$ is rather different from the others. The positive values in the central part indicate that the air tends to re-attach to the stator surface after it comes in around the corner. The right negative part on the curve represents the flow direction of the upper re-circulating

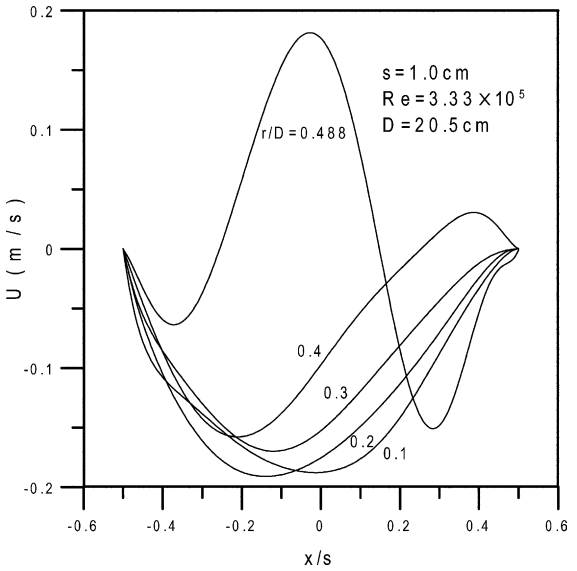

Fig. 6. Axial velocity component inside the gap between the rotor and the stator.

region. The left negative part on the curve reflects the prerequisite tendency of the stream before it is thrown out of the gap.

Fig. 7 gives the distributions of the azimuthal velocity W. Comparing to the radial velocity profile (Fig. 5) where there is a velocity cross-over point in $x/s = -0.14$, the velocity cross-over point in Fig. 7 is located about the mid-plane of the gap. The velocity values on the right half are below 2 m/s, while those on the left, i.e. near the rotating disk, are relatively much higher. Though they have the same feature of a high-velocity layer near the rotor wall, the distributions are quite different in view of the whole gap. For $r/D \geqslant 0.3$, the velocity declines gradually apart from the high-velocity thickness. But for smaller radii, the velocity is hardly changeable, which means that the fluid near the axis was rotating almost like a rigid body. In addition, the change of the velocity with radius for the right part is opposite to that for the left part. To the right of the cross-over point, the azimuthal velocity becomes smaller as the radius increases. It is nearly zero at $r/D = 0.488$. This reveals that for the fluid near the stator, the inner part rotates more strongly than the outer part near the edge of the disk.

For temperature distributions inside the gap, Fig. 8 plotted the excess temperature, $T - T_a$, used to indicate the temperature rise of the fluid. The profiles for different radii are similar. Most temperature drops happen within $x/D < 0.3$ from the stator surface. Then it climbs gradually towards the rotor. Because the isotherms in the gap take the U shape approximately and pile up from high to low (see Fig. 4(b)), it is not so hard to understand such temperature profiles shown in Fig. 8. Degrees of the temperature rise are quite different for different radii, with minimums from nearly zero of $r/D = 0.488$ to 6 °C of $r/D = 0.1$. This denotes the different heat transfer rate in different depth of the gap.

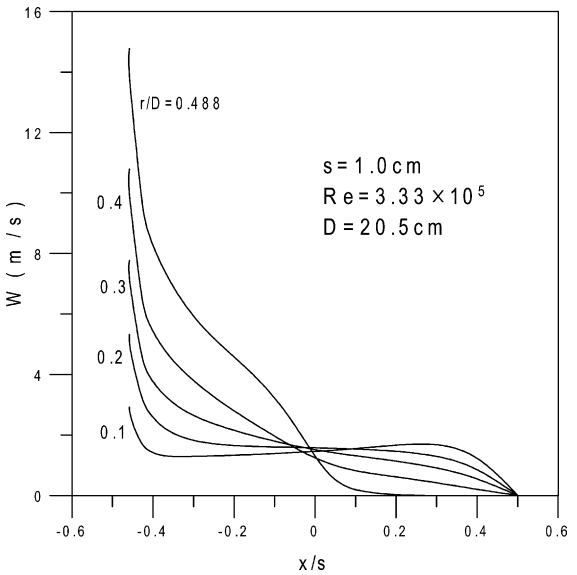

Fig. 7. Azimuthal velocity component inside the gap between the rotor and the stator.

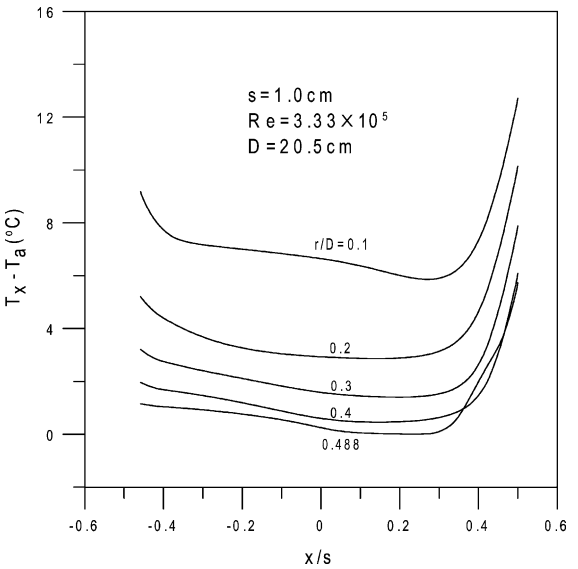

Fig. 8. Temperature profiles inside the gap between the rotor and the stator.

4.3. Local heat transfer characteristics

Fig. 9 shows the experimental results, cases of $s = 0.50, 0.75$ and 1.00 cm, along with the numerical results. It was difficult in the experiment to obtain meaningful data around the center of the disk because of low temperature gradient. Because the heat transfer tends to change complicatedly near the outer edge, as shown by the numerical results in the figure, the color pattern of the liquid crystal became less distinguishable. Therefore, only the experimental data in the range of $r/R = 0.24$–0.92 are available for the numerical results to compare with.

In general, trends of the experimental results are compatible to those of numerical simulations. The tendency of the Nusselt number for both results is consistent, though the experiments produced lower heat transfer rate than the simulation in most cases. For the case of $Re = 1.42 \times 10^5$, the simulation revealed that $s = 0.75$ cm has the best heat transfer performance, which is just the situation of the experimental data for $r/R > 0.6$. But for cases of $Re = 2.10 \times 10^5$ and 2.94×10^5, experimental results show that heat transfer decreases monotonically with the increase of the disk-distance, while by the numerical results the case of $s = 0.75$ cm remains the best within the range of the experimental parameters. Similar discrepancy exists in the case of $Re = 3.33 \times 10^5$. Another noteworthy point is the differences of Nusselt number for different disk-spaces in the simulated results. At lower Reynolds number, the differences of the numerical Nusselt number are less noticeable for $r/R < 0.9$. The difference lies mainly in the region near the edge. For higher Reynolds numbers, however, the difference at various disk-spaces is much more apparent.

4.4. Effect of the disk-distance

The effect of the distance has been a main focus during this investigation. Fig. 10, in which Reynolds number varied parametrically, shows the distributions of the local Nusselt number for different disk-distances. These distributions are based on the numerical results only. When the disk-distance changes from 0.25 to 1.0 cm, the distribution has changed not only for the values but also for the profile shapes. In general, the distributions of $s = 0.50$ and 0.75 cm show steeper slope in the whole radius range, meaning higher average heat transfer rate. The slope of the profile for $s = 1.00$ cm has deteriorated to some extent. The case of $s = 0.25$ cm presents the flattest distributions in all situations.

The shapes of the profiles are quite different from one another. There exists a peak and a valley in the distributions of $s = 0.75$ and 1.00 cm for a given Reynolds

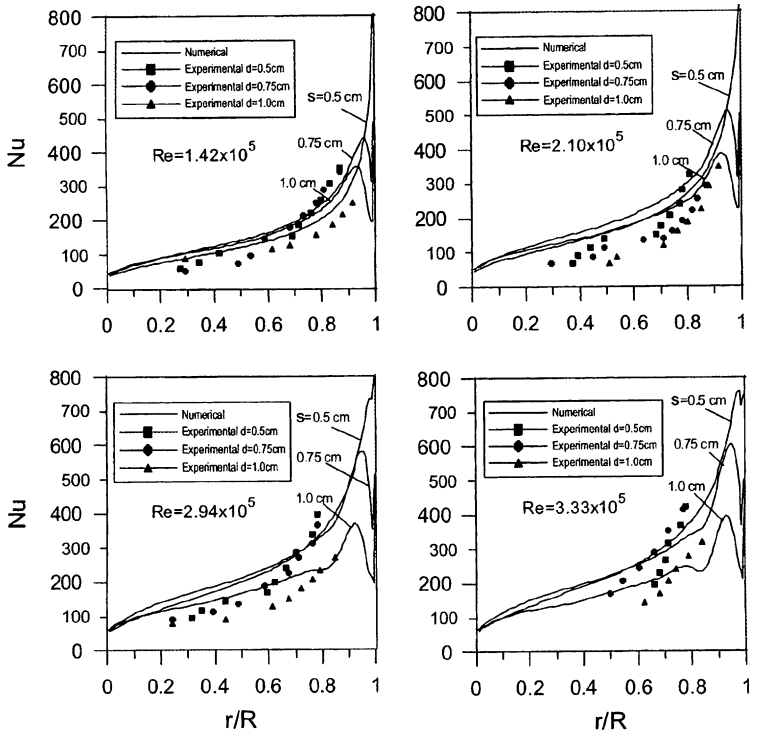

Fig. 9. Comparison of the experimental and numerical results of heat transfer.

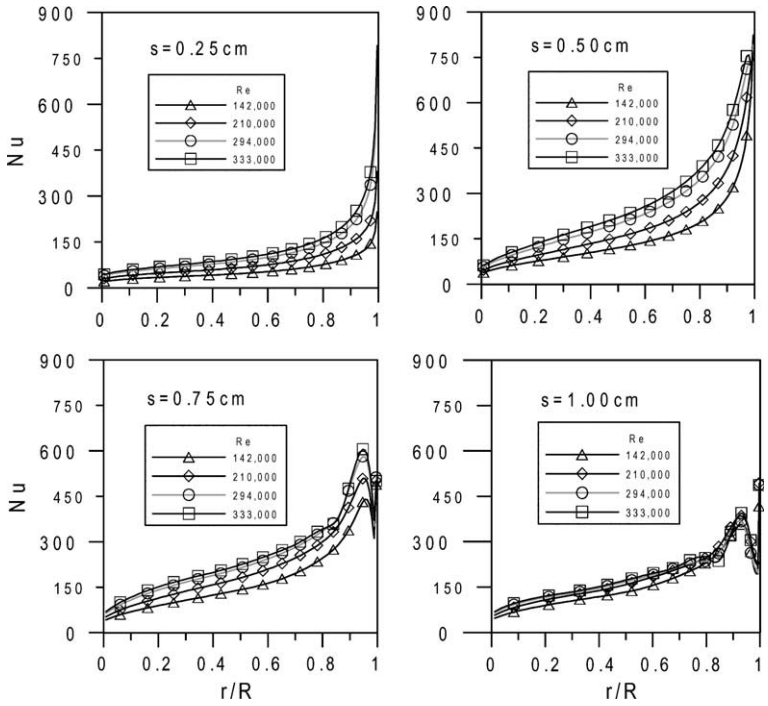

Fig. 10. Numerical distribution of the local Nusselt number for different disk-distances.

number. The valleys are very close to the outer edge of the disk, while the location of the peak is apparently away from the edge, it is approximately $r/R = 0.92$ and 0.95 for the cases $s = 1.00$ and 0.75 cm, respectively. No obvious shift of the peak takes place when Reynolds number changes for a given disk-distance. When the disk-distance decreases to 0.5 cm, only at $Re = 3.33 \times 10^5$ the feature of peak–valley has been observed, and the peak and valley moved further close to the outer edge. As the disk-distance changes to 0.25 cm, the phenomenon of peak–valley disappeared completely, but with more aggressive slope near to the edge. The small re-circulating bubble on the surface of the stator down into the gap (see Fig. 4(a)) is considered to be responsible for the phenomenon of the peak and valley. In general, there always exists a maximum of heat transfer wherever the flow re-attaches to the heated surface [31–33]. This is due to the location of the re-attachment is the whereabouts of the thinnest boundary layer, accordingly the location of the least thermal resistance. On the other hand, the bottom of the valley is consistent with the upper end of the re-circulating bubble, which stops at a small distance from the outer edge of the disk. As the disk-distance becomes small enough, the re-circulating bubble exists no longer so that the phenomenon of peak and valley disappears accordingly. It is interesting that Hill and Ball also found the similar peak phenomenon of heat transfer in their study about counter-rotating disks [24].

The Reynolds number displays different influence on the heat transfer when the disk-distance changes. According to the simulated results it is noted that the Reynolds number imposes less influence on heat transfer as the distance increases. From $s = 0.25$ to 1.00 cm, profiles of Nusselt number tend to cluster more closely. For the case $s = 1.00$ cm no significant difference among the runs of various Reynolds numbers can be detected. This implies that at larger disk-distances increasing Reynolds number is not an appropriate way any more to enhance the heat transfer in such a rotor–stator system.

For the purpose of identifying an optimum disk-distance for heat transfer, the average heat transfer rate on the surface has been used. Fig. 11 shows the variation of the average Nusselt number with the relative disk-distance for different Reynolds numbers. If the distance between the rotor and the stator is very large, the effect of the rotation of the rotor on the convective heat transfer of the stator would be definitely alleviated, because the interaction between these two disks would become insignificant. On the other hand, if the two disks are very close, the flow inside the gap would be similar to that of an infinite rotor–stator system, little mass of coolant air can get into the gap and penetrate the depth of it. Thus the heat transfer on the stator will degrade, too. Based on this analysis it can be expected that, for a fixed Reynolds number, there may exist a disk-distance at which the average heat transfer performance reaches its maximum. The results shown in Fig. 11 verified the

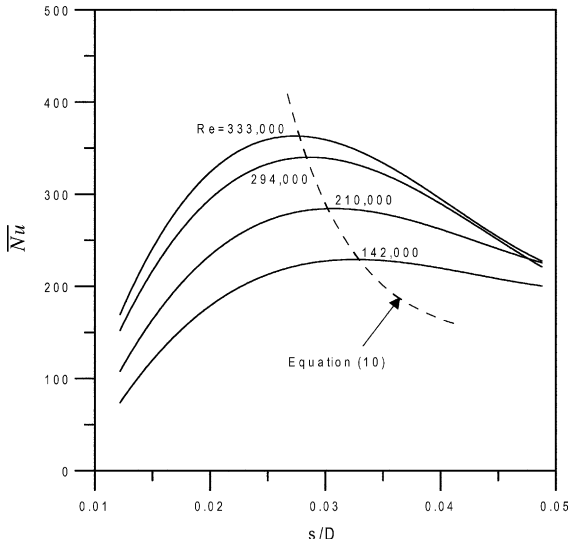

Fig. 11. Changes of the average heat transfer rate along the heated surface of the stationary disk at different Reynolds number.

analysis above. The maximum point of $\overline{Nu}$ for each given Reynolds number is apparent. However, its location shifts towards the smaller s values as Reynolds number increases. Also observed in Fig. 11 is the fact that the average heat transfer is more sensitive to disk-distances at smaller s values than at larger s values.

Correlated with least-square-fit method, the relationship between the average Nusselt number and the relative disk-distance as well as Reynolds number is as following

$$\overline{Nu} = -1.016Re^{0.4664} + 18.15Re^{0.6426}\left(\frac{s}{D}\right) - 126.3Re^{0.7485}\left(\frac{s}{D}\right)^2 + 707.5Re^{0.7749}\left(\frac{s}{D}\right)^3 \quad (9)$$

The error of correlation (9) is under 3%. The optimized disk-distance, at which the average heat transfer rate reaches its maximum for given Reynolds number, is also shown in a dashed line in the figure. The location for the maximum of the average heat transfer is correlated as

$$\left(\frac{s}{D}\right)_{\overline{Nu},\max} = Re^{-0.0264}\left[0.0595 - \sqrt{(3.541 - 8.551Re^{-0.0795}) \times 10^{-3}}\right] \quad (10)$$

5. Conclusions

Experiments and numerical simulations have been conducted to investigate the heat transfer and flow between a rotating and a stationary disk. With the blockage of the stationary disk, the flow pattern generated by the rotating disk shows an asymmetrical tendency. The main stream of the airflow tends to deflect towards the stator side. There exists a small re-circulating region on the surface of the stator, which is near the inlet of the gap. This small re-circulating region acts as an important role to the fluid flow inside the gap and the heat transfer on the stationary disk. The flow in the gap is basically a Stewartson-type, which means a boundary layer formed on the rotor wall but none on the stator wall. The numerical simulation showed a similar distribution of local heat transfer rate to that of experiment. In general, the numerical simulation produced higher heat transfer rate comparing to the experimental result. The discrepancy tends to increase with increasing Reynolds number. Based on the numerical results, the effect of the disk-distance and the rotational Reynolds number on the heat transfer on the stator has been discussed, and the relationship between the average Nusselt number and the two main influential factors, the relative disk-distance s/D and the Reynolds number Re, has been correlated. For a given Reynolds number there is a corresponding optimum disk-distance, at which the average heat transfer reaches its maximum. The maximum point moves towards the small disk-distance as the Reynolds number increases.

References

[1] J.M. Owen, R.H. Rogers, Flow and Heat Transfer in Rotating Disc Systems, vol. 1: Rotor–Stator Systems, Research Studies Press, John Wiley, New York, 1989.
[2] G.K. Batchelor, Note on a class of solutions of the Navier–Stokes equations representing steady rotationally-symmetric flow, Qly. J. Mech. Appl. Math. 4 (1951) 333–354.
[3] K. Stewartson, On the flow between two rotating coaxial disks, Proc. Cambridge Philos. Soc. 49 (1953) 333–341.
[4] P.J. Zandbergen, D. Dijkstra, Von Karman swirling flows, Ann. Rev. Fluid Mech. 19 (1987) 465–491.
[5] J.W. Daily, R.E. Nece, Chamber dimension effects on induced flow and frictional resistance of enclosed rotating disks, J. Basic Eng. 82 (1960) 217–228.
[6] P. Cooper, E. Reshotko, Turbulent flow between a rotating disc and a parallel wall, AIAA J. 13 (1975) 573–589.
[7] C. Wagner, Heat transfer from a rotating disk to ambient air, J. Appl. Phys. 19 (1948) 837–839.
[8] D.E. Metzger, Heat transfer and pumping on a rotating disk with freely induced and forced cooling, ASME J. Eng. Power 92 (1970) 342–348.
[9] N. Saniei, X. Yan, An experimental study of heat transfer from a disk rotating in an infinite environment including heat transfer enhancement by jet impingement cooling, Enhanced Heat Transfer 7 (2000) 231–245.
[10] F. Kreith, J.H. Taylor, J.P. Chong, Heat and mass transfer from a rotating disk, ASME J. Heat Transfer 81 (1959) 95–104.

[11] C. Prakash, U.S. Powle, N.V. Suryanarayana, Analysis of laminar flow and heat transfer between a stationary and a rotating disk, AIAA J. 23 (11) (1985) 1666–1667.
[12] H. Nesreddine, C.T. Nguyen, D. Vo-Ngoc, Laminar flow between a stationary and a rotating disk with radial throughflow, Numer. Heat Transfer, Part A 27 (1995) 537–557.
[13] A. Randriamampianina, L. Elena, J.P. Fontaine, R. Schiestel, Numerical prediction of laminar, transitional and turbulent flows in shrouded rotor–stator systems, Phys. Fluids 9 (6) (1997) 1696–1713.
[14] R. Pilbrow, H. Karabay, M. Wilson, J.M. Owen, Heat transfer in a "cover-plate" preswirl rotating-disk system, ASME J. Turbomach. 121 (1999) 249–256.
[15] C.M. Ellwood, W.J. Korchinsky, The heating, by viscous dissipation, of liquids flowing across an enclosed rotating disc, Int. J. Heat Mass Transfer 43 (2000) 1035–1050.
[16] Y.P. Dyban, V.Y. Kabkov, Experimental study of flow of air in a gap formed by two rotating disks, Fluid Mech.—Soviet Res. 8 (4) (1979) 99–104.
[17] C.A. Long, P.G. Tucker, Numerical computation of laminar flow in a heated rotating cavity with an axial throughflow of air, Int. J. Numer. Meth. Heat Fluid Flow 4 (1994) 347–365.
[18] C.Y. Soong, Theoretical analysis for axisymmetric mixed convection between rotating coaxial disks, Int. J. Heat Mass Transfer 39 (8) (1996) 1569–1583.
[19] W.M. Yan, C.Y. Soong, Mixed convection flow and heat transfer between two co-rotating porous disks with wall transpiration, Int. J. Heat Mass Transfer 40 (4) (1997) 773–784.
[20] W.M. Yan, K.T. Lee, Unsteady conjugated mixed convection flow and heat transfer between two co-rotating discs, Int. J. Heat Mass Transfer 40 (12) (1997) 2975–2988.
[21] M. Kilic, X. Gan, J.M. Owen, Transitional flow between contra-rotating disks, J. Fluid Mech. 281 (1994) 119–135.
[22] X. Gan, M. Kilic, J.M. Owen, Flow between contra-rotating discs, ASME J. Turbomach. 117 (1995) 299–305.
[23] S. Bhattacharyya, A. Pal, G. Nath, Unsteady flow and heat transfer between rotating coaxial disks, Numer. Heat Transfer, Part A 30 (1996) 519–532.
[24] R.W. Hill, K.S. Ball, Direct numerical simulations of turbulent forced convection between counter-rotating disks, Int. J. Heat Fluid Flow 20 (1999) 208–221.
[25] N. Saniei, S. Dini, Effect of height and geometry on local heat transfer and pressure drop in a channel with corrugated walls, Heat Transfer Eng. 14 (4) (1993) 19–31.
[26] S.J. Kline, F.A. McClintock, Describing uncertainties in single sample experiments, Mech. Eng. 75 (1953) 3–9.
[27] T.B. Gatski, M.Y. Hussaini, J.L. Lumley, Simulation and Modeling of Turbulent Flows, Oxford University Press, New York, 1996.
[28] M. Wolfshtein, The velocity and temperature distribution of one-dimensional flow with turbulence augmentation and pressure gradient, Int. J. Heat Mass Transfer 12 (1969) 301–318.
[29] H.C. Chen, V.C. Patel, Near-wall turbulence models for complex flows including separation, AIAA J. 26 (6) (1988) 641–648.
[30] S.V. Patankar, Numerical Heat Transfer and Fluid Flow, Hemisphere, Washington, DC, 1980.
[31] Z.X. Yuan, Numerical study of periodically turbulent flow and heat transfer in a channel with transverse fin arrays, Int. J. Numer. Meth. Heat Fluid Flow 10 (2000) 842–861.
[32] Z.X. Yuan, W.Q. Tao, Q.W. Wang, Numerical prediction for laminar forced convection heat transfer in parallel-plate channels with streamwise-periodic rod disturbances, Int. J. Numer. Meth. Fluids 28 (1998) 1371–1787.
[33] E.M Sparrow, W.Q. Tao, Symmetric vs asymmetric periodic disturbances at the walls of a heated flow passage, Int. J. Heat Mass Transfer 27 (11) (1984) 2133–2144.